PAPER

Check for updates

Targeted therapy for the treatment of gliomas with multifunctional orange emissive carbon dots†

Shuyao Liu, [ID] ab Zhuoling Zhong, [ID] ab Chuanwei Zhang,ab Yanqu Zhou,ab Chunmei Fuab and Xiaoping Xu*ab

As a nano-material, carbon dots have been extensively studied and applied in many ways. Herein, iron-doped orange emissive carbon dots (ICDs) were easily synthesized using the hydrothermal method and coupled with Trf and glucose oxidase (GOD) simply by virtue of the abundant functional groups on their surface. The resulting carbon dots were named IGTCDs. The obtained IGTCDs possessed targeting, therapeutic and imaging functions, achieving the enzymolysis of glucose, the decomposition of H_2O_2 and the release of reactive oxygen species (ROS) sequentially in gliomas as a multifunctional nano-catalyst, and achieving an efficient glioma targeted killing effect. On the basis of the ideal biocompatibility of the IGTCDs with a cell survival rate of over 85%, even at a high concentration (500 μg ml^{-1}), the IGTCDs, which were coupled substances present within the organism, glucose oxidase and transferrins, showed an obvious inhibitory effect on the growth of tumor cells, and the survival rate of the C6 cells was only 28.10% at 300 μg ml^{-1}. The highly efficient anti-tumor effect was further demonstrated in the treatment of mice suffering from glioma, and the tumor inhibition rate was increased to 56.21–98.32%. This safe and effective multifunctional tumor inhibitor could be conveniently synthesized in large quantities, verifying the feasibility of the anti-tumor therapy based on the tumor microenvironment (TME), creating a novel method for the application of carbon dots in tumor treatment and providing a novel, reasonable and effective method for the treatment of cancer and gliomas.

Introduction

Glioblastomas, a type of primary brain tumor, are characterized by having a low cure rate, poor prognosis, short survival time and so on. They are generally treated using radiotherapy and chemotherapy, which rarely completely eliminate the invasive growth of the tumor and cause obvious toxic side effects. These methods also lack effective and reasonable treatment means, therefore, the development of novel and efficient treatment methods is desirable.[1–3] Compared with normal tissues, the tumor microenvironment (TME) has unusual characteristics, such as internal hypoxia, interstitial hypertension and a hyper-inflammatory response, and is weakly acidic (pH = 6.0–6.5) owing to the Warburg effect resulting from the accumulation of lactic acid and a high glucose uptake.[4–6] This arises from the bypassed metabolism of glucose through glycolysis at the tumor site owing to the high enzyme activity of glucose-6-phosphate dehydrogenase and the rapid transportation of glucose *via* GLUT1.[7–10] Vigorous glucose-dependent glycolysis provides the

tumor cells with the energy to maintain a normal metabolism and proliferation, which could trigger the apoptosis of tumor cells when inhibited, meaning the normal energy supply is affected. Utilizing the properties of glucose metabolism and the subacidity in the TME, as well as the discrepancy between normal tissues, could enable the specific release of the drug or the transformation of the inherent substances at the nidus,[11,12] which simultaneously improves the treatment precision, enhancing the curative effect and reducing the side effects. Tumor specific imaging and treatment based on the characteristics of the microenvironment show significant potential, and several related studies on pH-responsive drug release and targeted vector construction in the microenvironment have been published.[13,14]

Carbon dots, an emerging fluorescent nano-material, are widely used in photoelectric, physical and chemical detection and biological imaging owing to their economical and available raw materials,[15–17] simple synthesis, excellent optical properties and biocompatibility, and are commonly used in blue and green fluorescence,[18,19] which restricts their applications in biological imaging as a long wavelength emission is required.[20–22] Traditional quantum dots are limited in biological applications owing to their inherent toxicity and rapid elimination.[23–25] In contrast, carbon-based dots (particle size: 1–10 nm), with a better biocompatibility, have abundant functional groups on

aWest China School of Pharmacy, Sichuan University Chengdu, Sichuan, 610041, P. R. China. E-mail: xuxp319@scu.edu.cn

bSichuan Research Center for Drug Precision Industrial Technology, West China School of Pharmacy, Sichuan University, Chengdu 610041, China

† Electronic supplementary information (ESI) available. See DOI: 10.1039/d1na00722j

the surface. Therefore, these functional groups can be simply modified to enhance the targeting, and carbon-based dots are considered as an ideal carrier with a high bioavailability, safety and stability. There have been comprehensive studies reported on carbon dots ranging from the loading of mitochondria for *in vitro* imaging, drug loading and release, to tumor therapy.[26–29]

In the treatment of glioma, the BBB (blood–brain barrier) penetration ability is one of the critical factors that is used to evaluate the effectiveness.[30–32] Compared with traditional nanomaterials, certain carbon dots are tumor-targeting in addition to enabling imaging functions. Moreover, the selectivity and BBB penetration ability can be enhanced significantly by modifying the tumor penetrating peptides, such as the GRD peptide, hyaluronic acid (HA) and transferrin or other tumor marker ligands.[33–35] These nanomaterials, with integrated imaging and targeting functions, are of vital significance in the treatment of tumors or other diseases, especially if they have simultaneous therapeutic effects. A selection of anti-tumor nanotherapies have been developed based on the characteristics of TME, which could enable tumor tracking imaging, diagnosis and treatment by constructing pH-sensitive nanocarriers.[4,6,13] Iron-doped nanoparticles, such as ferromagnetic nanoparticles (γ-Fe_2O_3 or Fe_3O_4 NPs) and amorphous FeO nanoparticles (AFeNPs), can be used as catalysts to trigger the Fenton-like reaction in acidic TME, producing H_2O_2 by the enzymolysis of glucose, and then releasing reactive oxygen species (ROS) (mainly $\cdot$OH, hydroxyl radicals) to induce the apoptosis of tumor cells.[6,36]

Herein, IGTCDs, a multifunctional nanomaterial that can simultaneously accomplish targeting of brain tumors, therapy and imaging, was constructed. In this nanomaterial, Trf modification endows the IGTCDs with the ability to target tumors and GOD (glucose oxidase) enables the decomposition of glucose at the tumor site and increases the level of H_2O_2 to induce tumor cell apoptosis, exerting a therapeutic effect. The orange fluorescence of the IGTCDs, which is different from the biological background, facilitates biological imaging and enables the simple observation of the metabolism, distribution and cellular uptake processes of the IGTCDs. This study verifies the feasibility of anti-tumor therapy based on the TME and the tumor tissue specific reaction could significantly reduce the side effects, enabling an ideal anti-tumor efficacy.

Experimental section

Fabrication of the IGTCDs

Tryptophan (0.05 g), 0.108 g *o*-phenylenediamine and 0.8 g $FeCl_3 \cdot 6H_2O$ were weighed and 200 µl of conc. hydrochloric acid and 10 ml H_2O was added. This mixture was dispersed evenly and transferred into a reaction kettle at 200 °C for 3 h to obtain a solution of the ICDs, after dialysis in ultrapure water for 10 h and freeze-drying, a reddish brown solid powder was acquired. 20 mg of the ICDs were dissolved in 2 ml ultrapure water with 15 mg of 1-ethyl-3-(3-dimethylaminopropyl)carbodiimide (EDC) and 10 mg *N*-hydroxysuccinimide (NHS), activated by ultrasound for 1 h, and then 1 ml polyethylene glycol (PEG) was added dropwise under stirring to obtain the PEGylation ICDs.

After that, 500 µl of a 20 mg ml^{-1} GOD solution was added dropwise and stirred overnight to enable full coupling with the ICDs. Trf (1.7 mg), EDC (4 mg) and NHS (6 mg) were dissolved in 500 µl of PBS, and then ultrasound was applied for 1 h, then the above mentioned ICDS-GOD solution was added dropwise, stirred for 24 h, and then it was dialyzed with ultrapure water for 10 h (MW = 100 KD), and then lyophilized to collect the IGTCDs powder. The powder was stored in a sealed container at −20 °C for later use.

Characterization

Tecnai G2 F20 S-TWIN transmission electron microscopy was used to determine the structure of the ICDs and the other series of conjugates. X-ray photoelectron spectroscopy (XPS) of the IGTCDs was measured using an AXIS supra. The optical properties of the IGTCDs and the related conjugates were characterized using infrared spectrophotometry, ultraviolet spectrometry and fluorescence spectrophotometry. The potentials of the ICDs and their conjugates were determined using a Zetasizer Nano ZS.

Michaelis–Menten kinetics

Sodium acetate buffer (110 µl, 10 mM), 30 µl of IGTCDs and 30 µl of H_2O_2 or glucose in a gradient concentration were added into 96-well plates in turn, incubated for 30 min, then 30 µl of 5 mM TMB was added and the optical density (OD) value was immediately detected ($\lambda = 652$ nm) over 40 min using a microplate reader. The V_0 (initial reaction velocity) is related to the A (absorbance), and the corresponding kinetic curve was obtained. The Michaelis–Menten constant (K_m) and the maximal velocity (V_{max}) were calculated *via* Lineweaver–Burk plotting.

Cell culture

The L929 fibroblasts, C6 glioma and C6-LUC cell lines were obtained from the State Key Laboratory of Biotherapy. The C6 glioma cells were cultured in Dulbecco's modified Eagle's medium (DMEM), containing 10% fetal bovine serum (FBS), 100 units per ml of streptomycin, and 100 units per ml of penicillin, supplied by GE Life Sciences Co. Ltd. The cell lines were incubated at a constant temperature of 37 °C and under 5% CO_2 in the incubator and were cultured for subsequent experiments by adding 0.25% trypsin, 10% FBS, and fresh DMEM high glucose medium.

Cytotoxicity and effectivity tests for the IGTCDs

For the cytotoxicity test *in vitro*, L929 cells were inoculated into 96-well plates at a density of 5000–6000 cells per well and incubated in DMEM for 12 h until the cells adhered. The original medium was discarded and replaced by 100 µl fresh DMEM per well, then the IGTCDs (0, 100, 200, 300, 400, and 500 µg ml^{-1}) were added in turn and incubated at 37 °C for 24 h. After that, the culture medium in the plate was discarded, and the cells were carefully rinsed with saline, followed by the addition of 90 µl DMEM and 10 µl of the Cell Counting Kit-8 (CCK8 assay)

into each well, and the cell viability was measured at $\lambda = 450$ nm over 4 h.

The effect of the IGTCDs on the C6 glioma cells was determined using the same method. C6 glioma cells were inoculated in 96-well plates at a density of 6000–10 000 cells per well and incubated in DMEM high glucose medium under different pH values (6.0 or 7.4) for 8–10 h until the cells adhered. The original medium was discarded and replaced by 100 μl fresh DMEM (pH = 6.0 or 7.4) per well, then IGTCDs (0, 100, 200, 300, 400, and 500 μg ml^{-1}) were added in turn and incubated at 37 °C for a certain amount of time. After that, the aforementioned cell media was discarded and the cells were carefully rinsed with saline, followed by the addition of 90 μl of DMEM and 10 μl of the CCK8 assay into each well, and the cell viability was measured at $\lambda = 450$ nm within 4 h.

Subcellular localization and ROS generation of the IGTCDs

The release of ROS on the cellular level was observed using confocal laser scanning microscopy (CLSM, FV 1000, Olympus). The C6 glioma cells were inoculated in a 6-well plate with a density of 150 000–200 000 cells per well and incubated in DMEM high glucose medium at a specific pH (6.0 or 7.4) for 12 h until they had adhered. The original medium was discarded and replaced by 1 ml fresh DMEM (pH = 6.0 or 7.4) per well, then the IGTCDs (50, 150, and 300 μg ml^{-1}) were added in turn and incubated at 37 °C for a certain period of time. After that, the aforementioned cell media was discarded and 1 ml of 10 μM DCFH-DA sample solution was added and incubated at 37 °C for 25 min. The cell medium in each well was discarded, and the cells were carefully rinsed with serum-free DMEM and PBS in turn to remove the excess probes. The morphology of the cells was fixed for 15 min with 500 μl 4% paraformaldehyde, discarded and then 500 μl of 1 μm DAPI reagent was added; this was discarded after 5 min and carefully washed with PBS. DAPI reagent was used to locate the nucleus (Ex/Em = 340/488 nm) and observe the cellular uptake of the IGTCDs (Ex/Em = 560/610 nm) and DCFH-DA was oxidized by ROS to form the DCF (Ex/Em = 488/525 nm).

Glioma model of mice

Female Kunming mice aged 4 weeks were purchased from Beijing HFK Bioscience Co., Ltd. All the animal procedures were performed under the protocols approved by the Department of Medical Animal Center, Sichuan University, and the experiments were performed in agreement with the guidelines of the Institutional Animal Care and Use Committee of Department of Medical Animal Center, Sichuan University.

Twenty-five female Kunming mice were fed adaptively for one week and were found to weigh 20–25 g. After being anesthetized with intraperitoneally injected 4% chloral hydrate (150 mg kg^{-1}), the mice were shaved carefully from the top of the head to the right ear and fixed on a stereotactic device in the prone position. After routine disinfection, a vertical incision with a length of about 1.0 cm was made from the ocular fissure at the midline, and the cranial parietal cross line was exposed. Drilling holes were made at 2.0 mm to the right side of the cross

center and then 0.6 mm of the lower side, with a diameter of about 1.0 mm. Then, C6-LUC cells (10 μl, 2.5×10^5 cells) were inoculated using a microsyringe. The affected area was sutured with absorbable sutures and the wound surface was disinfected. Five days after inoculation, the weight of the mice decreased slightly, foraging was normal, the frequency of drinking decreased, and the injection site in the head bulged slightly. The mice were grouped using the detected tumor signals. The mice were intraperitoneally injected with 150 mg kg^{-1} 4% chloral hydrate and D-luciferin potassium (Dalian Meilun Biotechnology Co., Ltd), then the tumor signals were observed and recorded using small animal living imaging (PerkinElmer I, VIS Lumina LT Series III) and labeled accurately.

Therapeutic effects of the IGTCDs

Nine mice with approximate tumor signals ($1.4–4.5 \times 10^6$) were screened and equally divided into experimental groups (high dosage and low dosage, $n = 3$) and the control group ($n = 3$). The experimental groups were injected with 300 μg ml^{-1} IGTCDs (3 and 6 mg kg^{-1}) *via* the tail vein at intervals of 24 h respectively, and the control group was injected with the equivalent amount of saline. 8–11d after inoculation, the mice in the control group were costive, tilted to one side and the top of the head were observed to bulge further, while no further aggravation was observed in the experimental groups. Up to 13–15 d, the mice in the control group presented disordered hair and had a listless spirit and an obvious bulge, while the morphological behavior of the mice in the experimental groups was normal. The tumor signals of the mice were recorded using the aforementioned method on days 10 and 15, respectively, the whole process was accurately documented and the changes in individual tumor signals were recorded.

Three female Kunming mice, weighing 20–25 g, were injected with ICDs (300 μg ml^{-1}, 3 mg kg^{-1}) *via* the tail vein for 10 d at intervals of 24 h respectively. The mice were sacrificed, and the tissues were dissected, then the distribution and brain targeting of ICDs was observed using living imaging with Ex/Em = 560/610 nm.

Statistical analysis

One-way analysis of variance (ANOVA) or t-test for multiple comparisons were used for statistical analysis. The data were expressed as mean ± standard deviation (SD) and the statistical significance was set at *$p < 0.05$, **$p < 0.01$ and ***$p < 0.001$.

Results & discussion

Therapeutic mechanism of the IGTCDs

Positively charged ICDs were successively coupled with GOD and Trf, and the IGTCDs obtained integrated the GOD activity, the Trf targeting function and the long wavelength emission (Ex/Em = 560/610 nm) of the ICDs, which constituted the basis of targeted therapy and imaging of glioma. Normal brain tissue with a dense microvessel endothelial space has a complete structure, resulting in poor penetration of macromolecules and lipid particles while the tumor tissue with rich vessels has

a broader space, less complete structure and worse lymphatic reflux, resulting in the high permeability and retention of macromolecules and lipid particles, called the EPR effect. The reason why macromolecular drugs are preferred for tumor therapy is not only due to the EPR effect, but also the non-specificity of small molecule drugs, which can freely pass through the vascular wall of normal and tumor tissues, then distribute indiscriminately, causing poor selectivity and toxic side-effects.[37–40]

Modified by GOD and Trf, the IGTCDs were negatively charged and the particle size increased to 100 nm, enabling them to effectively reach tumor tissues, actively target and specifically bind with transferrin receptors under the EPR effect, and enhance the tumor selectivity and therapeutic effect. A variety of GLUTs (glucose transporter) exist in tumor sites, vigorously uptaking glucose for proliferation and therefore resulting in a higher concentration of glucose at these sites compared to normal tissues. The IGTCDs can effectively target the nidus, hydrolyze glucose and produce H_2O_2, further realizing the catalytic decomposition of H_2O_2 and releasing ROS by the Fenton reaction in the weakly acidic conditions of the TME (pH = 6.0–6.5), which specifically increases the level of $\cdot OH$ in the affected area, regulating the apoptosis of tumor cells and inhibiting the metabolism of the tumor, achieving an ideal anti-tumor effect. If some of the IGTCDs begin to function before reaching the target, this would only result in acceptable and temporary decreases in the blood glucose levels and would have little effect on the H_2O_2 levels of normal tissues owing to the pH selectivity of the IGTCDs towards the catalytic reaction. The series of targeting, enzymatic hydrolysis and catalytic processes of the IGTCDs exhibited ideal tumor specificity and inhibition with few toxic and side effects on normal tissues and can be considered as a safe, effective and novel therapeutic form of treatment for gliomas or even other kinds of tumors.

Characterization of the IGTCDs

The fluorescence spectrum of the IGTCDs (Fig. 1a) shows that excitation at 560 nm can produce an orange fluorescence emission at 610 nm. The transmission electron microscopy (TEM) image shows that the IGTCDs were uniformly dispersed and had an approximate size of 100 nm (Fig. 1b). In the infrared spectrum (Fig. 1c), the O–H absorption at 3414.28 cm^{-1} and the C–O absorption at 1091.84 cm^{-1} demonstrated the existence of phenolic or alcoholic hydroxyl groups, the absorption at 1022.5 cm^{-1} was attributed to the ether bond of GOD. Moreover, the absorption peaks at 3414.20, 1647.28, 1295.66 and 1249.17 cm^{-1} indicate the generation of amide bonds, which cannot be seen in both ICDs or ICDs-GOD (S.2†), and may be related to the carboxyl of the transferrin binding with the amino group in the ICDs-GOD. The XPS (Fig. 1d) characterization results show that the IGTCDs contain C, O, Cl, N, Fe and other elements, and the divided peak of Fe 2p (S.1†) showed two strong absorption peaks at 712 and 725 eV, indicating the existence of Fe^{2+} and Fe^{3+}. There is a strong absorption peak at 430 nm in the ultraviolet image of the ICDs (Fig. 1e), indicating the existence of a n → π* transition, which may be related to

the C=O structure. In summary, the IGTCDs have hydroxyl and carboxyl groups, the ether and amide bonds and the doped iron mainly exist in the form of Fe^{2+} and Fe^{3+}, showing orange fluorescence under ultraviolet irradiation. S.2a† shows the TEM images of the ICDs coupled with GOD and Trf in turn. After coupling with GOD, the particle size increased to 50 nm, sequentially, the transferrin was coupled by the EDC/NHS reaction, and the obtained IGTCDs showed dispersed dendritic structures with an increased diameter up to 100 nm and the potential also changed. Owing to the electrostatic adsorption, electronegative transferrin can bind with the ICDs-GOD easily, the potential of the positively charged ICDs (3.58 mV) coupled with GOD decreased to 0.483 mV, and the negatively charged IGTCDs (−4.21 mV) were obtained after further modifying the Trf. The changes in the particle size and potential (S.2a and b†) during modification are beneficial to the specific distribution of the IGTCDs in tumor tissues.

Stability of the IGTCDs

Fig. 2a shows the DLS results for the IGTCDs, the particle size is 117.6 nm and the polydispersity index (PDI) is 0.282, indicating that the IGTCDs are well dispersed and uniform. The stability of the IGTCDs in PBS and 50% FBS were determined, and the particle sizes in different systems were determined at 12, 24, 36, 48, and 72 h respectively, as shown in Fig. 2b. The IGTCDs were basically stable in H_2O, 50% FBS and PBS with a uniform particle size distribution (PDI < 0.3), indicating that the dispersion of IGTCDs is good and stable.

Catalysis and fluorescence imaging function of the IGTCDs *in vitro*

As illustrated in the above section on the mechanism of the catalytic therapy, IGTCDs targeted the brain, initiated the enzymolysis of β-D-glucose in the tumor site, produced β-D-
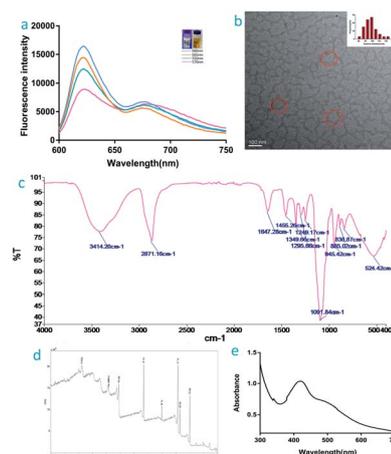

Fig. 1 Characterization of the IGTCDs: (a) fluorescence spectrum, the inset shows observation of the IGTCDs under ultraviolet and normal light. (b) TEM image. (c) The infrared spectrum. (d) The ultraviolet spectrum, and (e) XPS characterization of the IGTCDs (total elemental analysis, analysis of the divided peak of Fe 2p is attached in S.1†).
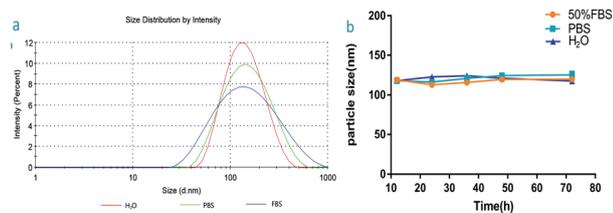
Fig. 2 (a) DLS of the IGTCDs in H$_2$O, PBS and 50% FBS after 72 h, the particle sizes are 117.6, 128,6 and 122.6 nm, respectively, and the PDI are all less than 0.3. (b) The particle size of the IGTCDs in H$_2$O, PBS and 50% FBS at different time points (12, 24, 36, 48 and 72 h).
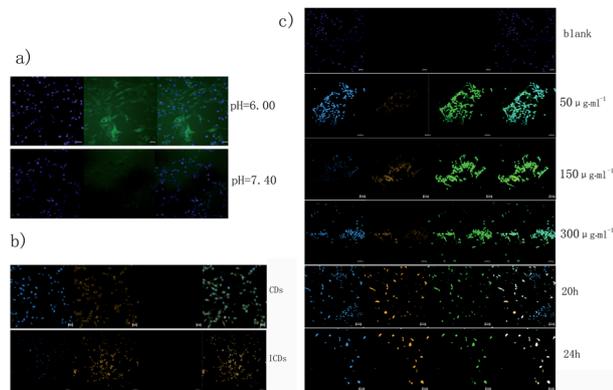

Fig. 3 Catalysis function of the IGTCDs *in vitro*: (a) the ROS release of the C6 cells catalyzed by IGTCDs at different pH values (6.00 and 7.40), detected by DCFH-DA and observed using CLSM with Ex/Em = 488/525 nm. (b) The detection of ROS released by C6 cells when incubated with CDs without iron-doping and ICDs (imaging performed after DAPI staining and observed under Ex/Em = 340/488 nm, the uptake of materials under Ex/Em = 560/610 nm, the DCFH-DA detection under Ex/Em = 488/525 nm and the merged image). (c) The detection of ROS released by C6 cells when incubated with IGTCDs for different periods of time (12, 20, and 24 h) or with different concentrations (0, 50, 150, 300 µg ml^{-1}) using DCFH-DA, the order of the graphs is the same as in (b).

glucose-1,5-lactone and H$_2$O$_2$, which was decomposed into toxic ˙OH by a Fenton-like reaction in the weakly acidic conditions of the TME and the main decomposition products in normal tissues (pH = 7.40), H$_2$O and O$_2$, were nontoxic. In order to determine the rate of production of the hydroxyl radical (˙OH), the DCFH-DA fluorescence probe was used to investigate the production of ROS in C6 glioma cells with different materials at different pH values, and CLSM was used to observe the production of ROS. As shown in Fig. 3a, there was an obvious green fluorescence observed in the cytoplasm under acidic conditions (pH = 6.00), suggesting that a large amount of ROS were generated in the cells, which oxidized the DCFH into fluorescent DCF, but neutral conditions (pH = 7.40) did not, indicating that the IGTCDs catalyzed the release of ˙OH at selected pH values.

The ROS release ability of the C6 cells catalyzed by CDs without iron doping and the ICDs without GOD coupling was measured using the same method, as shown in Fig. 3b. Green

fluorescence was not observed in either the CDs or ICDs, indicating that neither the CDs nor ICDs can enable the enzymatic hydrolysis of glucose or the decomposition of H$_2$O$_2$ to release ROS. However, orange fluorescence in the cytoplasm was observed at Ex/Em = 560/610 nm, indicating that carbon dots could be taken up by cells and were mainly distributed in the cytoplasm, which preliminarily verified the good biocompatibility and application of the probe in carbon dots. In order to determine the uptake of the IGTCDs, C6 cells were co-incubated with IGTCDs at different concentrations (50, 150, and 300 µg ml^{-1}) for 12 h, and the DCFH-DA fluorescence probe was added to observe the generation of ROS. Under acidic conditions (pH = 6.0), a strong green fluorescence could be observed in all IGTCDs groups, indicating the generation of ROS, which proved the eminent ability of the IGTCDs to catalyze the release of ROS by the enzymatic hydrolysis of glucose in an acidic environment. An obvious orange fluorescence was observed at Ex/Em = 560/610 nm, indicating that the IGTCDs could be effectively taken up by cells through endocytosis and distributed into the cytoplasm, which settled the basis of the intracellular effects and proved that IGTCDs are an excellent cell imaging material with a fluorescence that notably differs from that of the biological background.

Different concentrations of IGTCDs can produce high levels of ROS, but the number of cells in low concentrations of IGTCDs (50 µg ml^{-1}) were significantly greater than those observed in medium and high concentrations, which may be related to the apoptosis induced by ROS. Therefore, prolonging the co-incubation time of the IGTCDs (300 µg mL^{-1}) with C6 cells, from 12 h to 20 h and then to 24 h, the orange fluorescence is obviously boosted, indicating the better uptake of IGTCDs by the cells, which could further increase the ROS level and produce the desired effects. At this time, the number of cells decreased sharply, and the morphology of the cells changed obviously, from the initially observed shuttle deformation to round, which is related to the destruction of the cell membrane, and lipid oxidation and apoptosis induced by the strongly oxidizing ˙OH.[6,41,42]

In conclusion, IGTCDs have excellent optical properties and biocompatibility, can be distributed in cytoplasm by endocytosis, and the orange emission (Ex/Em = 560/610 nm) means they are excellent fluorescent probes that can be used for cell imaging. In addition, under acidic conditions, 300 µg ml^{-1} IGTCDs can effectively catalyze the enzymolysis of glucose and the release of ROS, producing highly toxic ˙OH by triggering the Fenton reaction to induce the apoptosis of C6 glioma cells, which preliminary proves the tumor killing effect at a cellular level.

In vitro catalytic performance of the IGTCDs

To further clarify the catalytic function of the material, 3,3′,5,5′-tetramethyl-benzidine (TMB) was used to monitor the production of radicals (Fig. 4). The produced hydroxyl radicals from the disproportionation of H$_2$O$_2$ under catalysis by the IGTCDs in acidic conditions oxidizes colorless TMB to chromogenic TMB cation-free radicals, which can be detected using

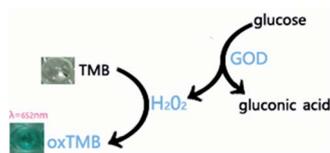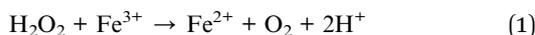**Fig. 4** The reaction mechanism of TMB (oxidized by H_2O_2, colorless TMB transforms to the chromogenic TMB cation-free radical, demonstrating absorption at $\lambda = 652$ nm).

a spectrophotometer at 652 nm. The mechanism of the Fenton reaction is as follows.

$$H_2O_2 + Fe^{3+} \rightarrow Fe^{2+} + O_2 + 2H^+ \tag{1}$$

$$Fe^{2+} + H_2O_2 \rightarrow Fe^{3+} + \cdot OH^- + \cdot OH \tag{2}$$

$$O_2 + Fe^{2+} \rightarrow Fe^{3+} + O_2 \tag{3}$$

Based on the aforementioned principles, typical Michaelis–Menten steady-state kinetics were applied to investigate the catalytic functionalities and performances of the IGTCDs. IGTCDs, H_2O_2 or glucose were successively added into 10 mM sodium acetate buffer, and 5 mM TMB was added after incubation at a certain temperature. As shown in Fig. 5, the UV absorption peak at 652 nm gradually increased and tended to be stable up to 40 min, indicating that the reaction had ended.

The conditions for the IGTCDs catalyzing the enzymatic reactions of H_2O_2, and glucose were optimized and the Michaelis–Menten steady-state kinetics of IGTCDs were determined. The optimum conditions for the enzymatic reaction of the IGTCDs were screened (S.3†), under which the following measurements of the kinetic constants of enzymatic activity were conducted. The detection of H_2O_2 was performed at 40 °C, pH 4.5 with 0.05 mM of IGTCDs and that of β-D-glucose was performed at 40 °C, pH 4.0 with 0.008 mM of IGTCDs. The time-course absorbance upon the addition of H_2O_2 or glucose into IGTCDs in sodium acetate buffer was plotted and is shown in Fig. 6 and the corresponding average initial velocities were calculated, respectively.
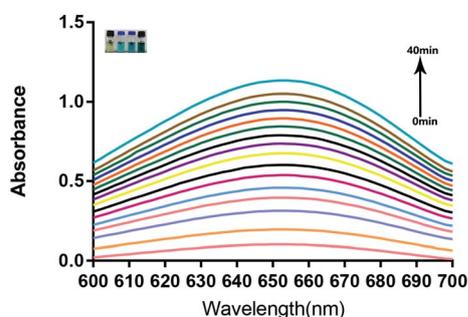

Fig. 5 The Fenton reaction monitored by the TMB color reaction and the absorbance at $\lambda = 652$ nm in 40 min. The inset shows the reaction system at the end and the degree of the color was positively correlated with the concentration of H_2O_2.
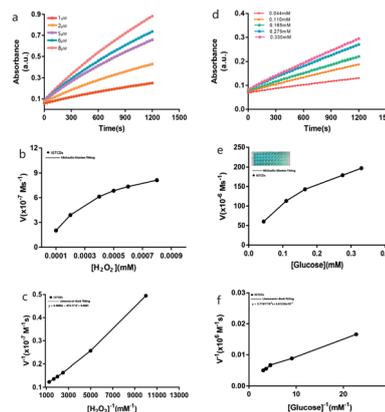

Fig. 6 *In vitro* catalytic performances of the IGTCDs. Time-course absorbance of IGTCDs upon the addition of various concentrations of (a) H_2O_2 (1, 2, 5, 6, and 8 μM) and (d) β-D-glucose (0.044, 0.110, 0.165, 0.275, and 0.330 mM). The Michaelis–Menten steady-state kinetics and Lineweaver–Burk plot of the IGTCDs for H_2O_2 (b) and (c) and β-D-glucose (e) and (f). The inset of (e) shows the chromogenic result at the endpoint of the catalytic reaction (the concentration of β-D-glucose decreased from left to right). The initial velocities were calculated within 180 s in one experiment.

According to the Beer–Lambert law (Fig. 7), the average initial absorbance changes are converted to the initial velocities (v_0) for the formation of cationic radicals or hydroxyl radicals, which were then plotted against the corresponding concentration and fitted with Michaelis–Menten curves. The linear double reciprocal plot (Lineweaver–Burk plot) was obtained and is shown in Fig. 5c and the K_m and V_{max} values were found to be 5.78×10^{-4} mM and 1.48×10^{-3} M s^{-1}.

For the glucose catalysis, the photograph in the inset of Fig. 6e visually presents the chromogenic changes after 1200 s upon the addition of glucose at various concentrations. The Michaelis–Menten curves and linear double reciprocal plot are displayed in Fig. 6f, and the K_m and V_{max} values were calculated to be 0.158 mM and 276.81 M s^{-1}, respectively.

The K_m value of the IGTCDs for glucose catalysis demonstrated that the nanocatalysts would present 50% of the maximum catalytic activity under 0.158 mM β-D-glucose, which suggested the ideal therapeutic effect towards common tumor cells as the endogenous glucose concentration was approximately 10 times greater and the concentration of IGTCDs in the actual treatment was also higher than that *in vitro*.[43] Above all, the peroxidase activity of the IGTCDs was verified. In addition, it

$$A = kbc$$

$$v_0 = \frac{V_{max} \cdot [S]}{K_M + [S]}$$

$$\frac{1}{v_0} = \frac{K_M}{V_{max}} \cdot \frac{1}{[S]} + \frac{1}{V_{max}}$$

Fig. 7 The Beer–Lambert law.

has been confirmed that the generation of $^1O_2$ during the catalysis of H_2O_2 by IGTCDs may be related to the electron transmission between H_2O_2 and IGTCDs (S.4†).

In vitro cytotoxicity and the effect of the IGTCDs

The aforementioned CLSM observations have verified that the IGTCDs could produce toxic hydroxyl radicals effectively and induce apoptosis in the acidic conditions of the TME. L929 and C6 cells were co-incubated with gradient concentrations of IGTCDs, respectively, to further evaluate the toxicity and effects using the CCK8 reagent in acidic or neutral conditions. As shown in Fig. 8a, the IGTCDs demonstrate little toxicity towards normal cells when cultured for 24 h in a neutral medium (pH = 7.4), and even at a higher concentration (500 μg ml^{-1}) the cell viability is still greater than 85%, indicating that the IGTCDs have good biological safety. However, upon incubation with C6 cells IGTCDs (100, 200, 300, 400 and 500 μg ml^{-1}) showed obvious cytotoxicity (Fig. 8b), and the cell viabilities (56.44, 43.44, 28.09, 26.37, 18.91%) under acidic (pH = 6.0) and neutral conditions (72.84, 61.13, 64.43, 57.27 and 51.46%) demonstrated significant differences ($p < 0.001$), showing that the IGTCDs could precisely induce the apoptosis of tumor cells in an acidic environment.

Upon co-incubation with an equivalent concentration of IGTCDs under neutral conditions, the discrepancy between the viability of the L929 and C6 cells may be a result of the higher concentration of β-D-glucose in tumor cells triggering the enzymatic catalysis of IGTCDs and producing a lethal hydroxy radical. Therefore, some tumor suppressive effects of IGTCDs were displayed even in a neutral culture environment and the neutral environment and low glucose levels of normal tissues limited the effects of the IGTCDs.

It can be seen that the IGTCDs presented a slight difference when the incubation time was extended from 12 to 36 h, and the cell viability at 36 h was mildly higher than that observed for 12
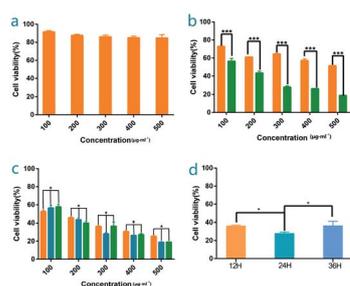
and 24 h. However, there were no significant differences ($p < 0.05$), indicating that the effect of the IGTCDs rapidly changed with minor time differences, and inhibited tumor growth to some extent. The tumor inhibition rate was 71.90% when incubated with 300 μg ml^{-1} of the IGTCDs for 24 h. Based on the results of the cytotoxicity study and the resulting effect, 300 μg ml^{-1} of IGTCDs with a low toxicity and ideal tumor inhibition rate were selected for further experiments.

Therapeutic effect of the IGTCDs *in vivo*

The transferrin receptors on the surface of the tumor cells (transferrin receptor, TfR) are 2–7 fold greater than those of the normal cells, meaning that the conjunction between the transferrin and TfR on the tumor cell surface is 10–100 fold greater than on normal cells. Transferrin-related agents can accumulate rapidly and be detained at the tumor sites and the therapeutic drugs can be specifically transported into tumor cells, thus bringing about the effect, which can be achieved by active targeting of the transferrin and transferrin receptor transport pathway (TF-TFR).[44–46] The ability of the IGTCDs to induce apoptosis of C6 glioma cells *in vitro* has been proved, and on this basis, the anti-tumor effect *in vivo* and the brain targeting of IGTCDs were further investigated. C6-LUC glioma
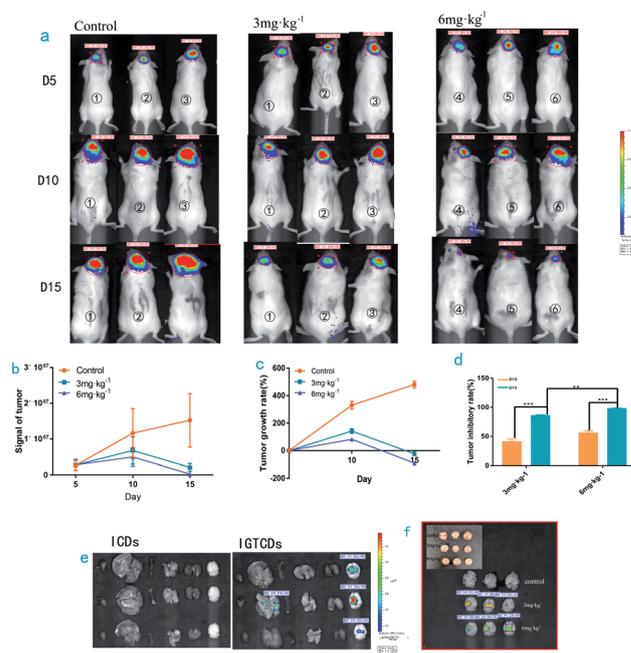

Fig. 9 *In vivo* catalytic–therapeutic performance and the tissue imaging of IGTCDs. Changes in the glioma signals in each group after inoculation with C6-LUC cells, observed after intraperitoneal injection of 150 mg kg^{-1} D-fluorescein potassium salt using living imaging on days 5, 10 and 15, respectively. (a) *In vivo* imaging and (b) the resulting variation curve. (c) The tumor growth rate within 15 d. (d) The tumor inhibitory rate within 15 d (** means $p < 0.01$ and *** means $p < 0.001$). (e) The tissue distribution of the ICDs and IGTCDs *in vivo*, the brains of the IGTCDs group presented fluorescence signals under Ex/Em = 560/610 nm. (f) Brain fluorescence signals of the IGTCDs in the control and therapeutic groups and the inset shows the morphology of the brains.

Fig. 8 *In vitro* cytotoxicity and intracellular catalytic performances of the IGTCDs. (a) The cytotoxicity profiles for L929 cells of the IGTCDs at various concentrations (pH = 7.40). (b) The cytotoxicity of the IGTCDs towards C6 cells at different pH values (7.40 and 6.00, $n = 3$). (c) The C6 cell viabilities with different incubation times (12, 24 and 36 h from the left, 12 h were 52.65, 45.56, 36.33, 30.74, and 25.48%, 24 h were 56.44, 43.44, 28.09, 26.37 and 18.91% and 36 h were 57.71, 40.02, 36.62, 27.31 and 19.03% in 200, 300, 400 and 500 μg ml^{-1} IGTCDs, $n = 3$ and * means $p < 0.05$, ***$p < 0.001$). (d) The viability of the C6 cell when incubated with 300 μg ml^{-1} IGTCDs for 12, 24 and 36 h ($n = 3$, 36.33 ± 0.76, 28.09 ± 1.37, 36.62 ± 4.54%).

cells labeled with luciferase were inoculated into the frontal lobe of mice using a stereotactic device to establish the glioma model. After adaptive feeding for 5 d, mice were intraperitoneally injected with 150 mg kg^{-1} D-fluorescein potassium salt and the tumor signals were actively recorded *in vivo*, before being screened and labeled for grouping. The therapeutic performances were investigated by administration of an equivalent amount of saline (control group, $n = 3$) and IGTCDs at different dosages (3 and 6 mg kg^{-1}, therapeutic groups, $n = 3$) intravenously and the resulting tumor signals were measured using the same method 5 and 10 d after administration. The mice were executed, and the tissues were dissected to determine the distribution of IGTCDs using living imaging.

It can be seen from the tumor signal–time diagram shown in Fig. 9a and from Table 1, that the control group was 4.30 (10 d) and 5.82 (15 d) times the original signal and the therapeutic groups were 2.43, 0.76 (3 mg kg^{-1}, low dose group) and 1.83, 0.09 times (6 mg kg^{-1}, high dose group) their original value, respectively. Moreover, the tumor inhibition rate was up to 41.45–98.32% (Table 2), indicating that the IGTCDs had an obvious antitumor effect and could effectively induce the apoptosis of glioma cells *in vivo*. Moreover, there is significant difference between the tumor inhibitory rates within 10 and 15 d of both the low and high dosage ($p < 0.001$) and there is less difference between the therapeutic groups ($P < 0.01$), indicating that the IGTCDs could enable an ideal inhibition even at low concentrations. As shown in Fig. 9f, under the fluorescence of the IGTCDs at Ex/Em = 560/610 nm, the distribution was concentrated in the brain and was obviously stronger than that observed in other tissues. In addition, the morphology of the brain observed in the control group in the inset of Fig. 9f was severely damaged, and the therapeutic groups were complete and demonstrated a better morphology, proving that the
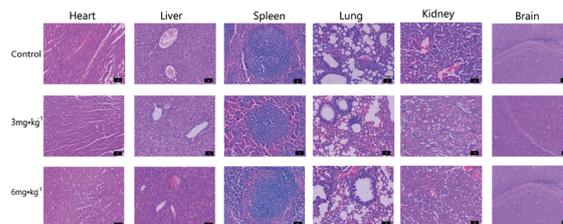

Fig. 10 Histopathology images of the dissected major organs (brain, heart, liver, spleen, lung and kidney) from the control and experimental groups stained using hematoxylin and eosin (H&E) for evaluation of the *in vivo* biosafety. Scale bar: 10 μm.

IGTCDs could inhibit the growth of the glioma and restore the normal structure of the brain.

The ideal glioma inhibitory effect of the IGTCDs is based on the targeted catalysis of glucose decomposition at the nidus, raising toxic hydroxyl radical levels *via* Fenton's reaction and inducing apoptosis of the glioma cells, therefore, the effective brain targeting of IGTCDs is the key to evaluating the therapeutic effect. Three mice were intravenously injected with ICDs (300 μg ml^{-1}, 3 mg kg^{-1}) at 24 h intervals, and the tissues were dissected 10 d later to observe the distribution of the ICDs. It can be seen in Fig. 9d, compared with the three mice in the therapeutic group (300 μg ml^{-1}, 3 mg kg^{-1}), that the ICDs do not target the brain, while IGTCDs have a significantly higher biological contrast distribution in the brain, which indicates that the transferrin has been effectively coupled, providing the basis for IGTCDs to reach the target. These results confirmed that the IGTCDs have admirable bioimaging and targeting functions towards gliomas and are a kind of catalytic nanomaterial that combine targeting, imaging and treatment abilities with a good biocompatibility.

Hematoxylin and eosin

The histopathology images of the dissected major organs were used to evaluate the pathological damage of IGTCDs on the brain and major organs. As shown in Fig. 10, the long spindle glioblasts of the control were arranged in parallel, and wavy palisade structures could be observed. These improved in the therapeutic groups, indicating the effect of the IGTCDs. Otherwise, there was no significant damage observed when compared with the control, further demonstrating the high biocompatibility of the IGTCDs during the therapeutic process.

Conclusion

Synthesized using the hydrothermal method, ICDs have rich functional groups on the surface and are easy to modify. These ICDs were coupled with GOD and Trf to obtain the IGTCDs, which enable targeting of the brain, glucose oxidase activity, orange fluorescence emissions, a low toxicity and good biocompatibility of the carbon dots on the whole. The IGTCDs could target the brain and take advantage of the characteristics of the TME to initiate a series of reactions including enzymolysis of glucose, decomposition of H_2O_2 and the release of ROS

Table 1 Tumor inhibition rate of the IGTCDs groups ($n = 3$)

Day	Tumor inhibition rate (%) 3 mg kg^{-1}	6 mg kg^{-1}
10	41.45	86.37
15	56.21	98.32

Table 2 Signals for the glioma in each group ($n = 3$)

Signal	Number	D5	D10	D15
Control	1	1 524 000	6 294 000	9 278 000
	2	2 236 000	9 280 000	12 790 000
	3	4 181 000	19 370 000	23 630 000
3 mg kg^{-1}	1	1 571 000	3 524 000	1 280 000
	2	2 271 000	5 845 000	1 638 000
	3	4 465 000	10 980 000	3 379 000
6 mg kg^{-1}	4	1 469 000	2 802 000	136 500
	5	2 350 000	4 314 000	189 200
	6	4 509 000	7 817 000	495 700

(˙OH), consuming the glucose in the tumor site, weakening glycolysis and inhibiting tumor metabolism and proliferation, and finally inducing the apoptosis of tumor cells at the nidus, thus realizing the targeted treatment of gliomas. The IGTCDs demonstrated a good peroxidase activity and biocompatibility. In addition, they facilitated cellular uptake and bioimaging using the orange fluorescence emission, presenting a high cell affinity and a good brain targeting function. Finally, IGTCDs demonstrated an ideal tumor inhibitory rate, integrating targeting, therapy and imaging functions together. Furthermore, they were conveniently synthesized and had an ideal efficacy. Herein, an ideal tumor inhibitor was obtained, and the feasibility of the anti-tumor therapy based on the TME was verified. Furthermore, this study details a novel idea for the application of carbon dots in tumor therapy. Considering the common characteristics of the TME in tumor tissues, this method may be effective in the treatment of other kinds of tumors.

Conflicts of interest

There are no conflicts to declare.

References

1 D. Srikanthan, M. S. Taccone, R. Van Ommeren, J. Ishida, S. L. Krumholtz and J. T. Rutka, *Chin. Neurosurg. J.*, 2021, **7**, 6.

2 S. Gui, P. Chen, Y. Liu, Q. Chen, T. Cheng, S. Lv, T. Zhou, Z. Song, J. Xiao, W. He, S. Yuan and Z. Cheng, *Biochem. Biophys. Res. Commun.*, 2021, **577**, 130–138.

3 Z. Zhao, K.-N. Zhang, Q. Wang, G. Li, F. Zeng, Y. Zhang, F. Wu, R. Chai, Z. Wang, C. Zhang, W. Zhang, Z. Bao and T. Jiang, *Genomics, Proteomics Bioinf.*, 2021, **19**, 1–12.

4 J. Fu, Y. Shao, L. Wang and Y. Zhu, *Nanoscale*, 2015, **7**, 7275–7283.

5 P. Mi, D. Kokuryo, H. Cabral, H. Wu, Y. Terada, T. Saga, I. Aoki, N. Nishiyama and K. Kataoka, *Nat. Nanotechnol.*, 2016, **11**, 724–730.

6 L. Liang, L. Wen, Y. Weng, J. Song, H. Li, Y. Zhang, X. He, W. Zhao, M. Zhan, Y. Li, L. Lu, Y. Xin and C. Lu, *Chem. Eng. J.*, 2021, **425**, 131451.

7 K. Tilekar, N. Upadhyay, C. V. Iancu, V. Pokrovsky, J. Y. Choe and C. S. Ramaa, *Biochim. Biophys. Acta, Rev. Cancer*, 2020, **1874**, 188457.

8 Y. Liu, Y. M. Li, R. F. Tian, W. P. Liu, Z. Fei, Q. F. Long, X. A. Wang and X. Zhang, *Brain Res.*, 2009, **1304**, 149–154.

9 A. Azzalin, G. Nato, E. Parmigiani, F. Garello, A. Buffo and L. Magrassi, *Neoplasia*, 2017, **19**, 364–373.

10 P. Koppula, K. Olszewski, Y. Zhang, L. Kondiparthi, X. Liu, G. Lei, M. Das, B. Fang, M. V. Poyurovsky and B. Gan, *iScience*, 2021, **24**, 102649.

11 K. Sasaki, S. Nishina, A. Yamauchi, K. Fukuda, Y. Hara, M. Yamamura, K. Egashira and K. Hino, *Cell. Mol. Gastroenterol. Hepatol.*, 2021, **11**, 739–762.

12 L. N. Raines and S. C. Huang, *Cancer Cell*, 2021, **39**, 907–909.

13 C. Zhang, W. Bu, D. Ni, S. Zhang, Q. Li, Z. Yao, J. Zhang, H. Yao, Z. Wang and J. Shi, *Angew. Chem., Int. Ed.*, 2016, **55**, 2101–2106.

14 L. Qiao, T. Sun, X. Zheng, M. Zheng and Z. Xie, *Mater. Sci. Eng., C*, 2018, **85**, 1–6.

15 S. Li, Z. He, Y. Li, K. Liu, M. Chen, Y. Yang and X. Li, *J. Alloys Compd.*, 2022, **889**, 161561.

16 K. K. Gudimella, G. Gedda, P. S. Kumar, B. K. Babu, B. Yamajala, B. V. Rao, P. P. Singh, D. Kumar and A. Sharma, *Environ. Res.*, 2021, **204**, 111854.

17 S. Sri, G. B. V. S. Lakshmi, P. Gulati, D. Chauhan, A. Thakkar and P. R. Solanki, *Anal. Chim. Acta*, 2021, **1182**, 338909.

18 S. Chattopadhyay, N. Mehrotra, S. Jain and H. Singh, *Microchem. J.*, 2021, **170**, 106706.

19 R. Bhuyan, K. Bramhaiah and S. Bhattacharyya, *J. Colloid Interface Sci.*, 2021, **605**, 364–372.

20 H. Li, H. Wang, J. Guo, S. Ye, W. Shi, X. Peng, J. Song and J. Qu, *Sens. Actuators, B*, 2020, **311**, 127891.

21 Y. Jiao, Y. Meng, W. Lu, Y. Gao, Y. Liu, X. Gong, Y. Liu, S. Shuang and C. Dong, *Talanta*, 2020, **219**, 121170.

22 A. Lv, Q. Chen, C. Zhao, S. Li, S. Sun, J. Dong, Z. Li and H. Lin, *Chin. Chem. Lett.*, 2021, DOI: 10.1016/j.cclet.2021.06.020.

23 A. Kumar and P. Kumar, *J. Hazard. Mater.*, 2021, **402**, 123777.

24 M. A. Farzin and H. Abdoos, *Talanta*, 2021, **224**, 121828.

25 Z. Wang and M. Tang, *Environ. Res.*, 2021, **194**, 110593.

26 Y. Sun, S. Liu, L. Sun, S. Wu, G. Hu, X. Pang, A. T. Smith, C. Hu, S. Zeng, W. Wang, Y. Liu and M. Zheng, *Nat. Commun.*, 2020, **11**, 5591.

27 S. Rai, B. K. Singh, P. Bhartiya, A. Singh, H. Kumar, P. K. Dutta and G. K. Mehrotra, *J. Lumin.*, 2017, **190**, 492–503.

28 S. A. Mathew, P. Praveena, S. Dhanavel, R. Manikandan, S. Senthilkumar and A. Stephen, *RSC Adv.*, 2020, **10**, 24386–24396.

29 W. Q. Li, Z. Wang, S. Hao, L. Sun, M. Nisic, G. Cheng, C. Zhu, Y. Wan, L. Ha and S. Y. Zheng, *Nanoscale*, 2018, **10**, 3744–3752.

30 Y. Wei, Y. Sun, J. Wei, X. Qiu, F. Meng, G. Storm and Z. Zhong, *J. Controlled Release*, 2021, **337**, 521–529.

31 C. S. Lee and K. W. Leong, *Curr. Opin. Biotechnol.*, 2020, **66**, 78–87.

32 S. Reddy, K. Tatiparti, S. Sau and A. K. Iyer, *Drug Discovery Today*, 2021, **26**, 1944–1952.

33 M. Zhang, X. Zhao, Z. Fang, Y. Niu, J. Lou, Y. Wu, S. Zou, S. Xia, M. Sun and F. Du, *RSC Adv.*, 2017, **7**, 3369–3375.

34 S. Li, D. Amat, Z. Peng, S. Vanni, S. Raskin, G. De Angulo, A. M. Othman, R. M. Graham and R. M. Leblanc, *Nanoscale*, 2016, **8**, 16662–16669.

35 L. Gao, X. Zhao, J. Wang, Y. Wang, L. Yu, H. Peng and J. Zhu, *Opt. Mater.*, 2018, **75**, 764–769.

36 L. Xu, J. Wang, J. Wang, S.-Y. Lu, Q. Yang, C. Chen, H. Yang, F. Hong, C. Wu, Q. Zhao, Y. Cao and H. Liu, *Chem. Eng. J.*, 2022, **427**, 131671.

37 J. Shi, P. W. Kantoff, R. Wooster and O. C. Farokhzad, *Nat. Rev. Cancer*, 2017, **17**, 20–37.

38 V. Torchilin, *Adv. Drug Delivery Rev.*, 2011, **63**, 131–135.

39 H. Maeda, *J. Controlled Release*, 2012, **164**, 138–144.

40 H. Maeda, H. Nakamura and J. Fang, *Adv. Drug Delivery Rev.*, 2013, **65**, 71–79.

41 Y. Hao, Z. Dong, M. Chen, Y. Chao, Z. Liu, L. Feng, Y. Hao, Z. L. Dong, M. C. Chen, Y. Chao, Z. Liu and L. Z. Feng, *Biomaterials*, 2020, **228**, 119568.

42 W. Yang, N. Oturan, S. Raffy, M. Zhou and M. A. Oturan, *Chem. Eng. J.*, 2020, **383**, 123155.

43 R. A. Nascimento, R. E. Ozel, W. H. Mak, M. Mulato, B. Singaram and N. Pourmand, *Nano Lett.*, 2016, **16**, 1194–1200.

44 A. Kano, K. Moriyama, T. Yamano, I. Nakamura, N. Shimada and A. Maruyama, *J. Controlled Release*, 2011, **149**, 2–7.

45 S. Tortorella and T. C. Karagiannis, *J. Membr. Biol.*, 2014, **247**, 291–307.

46 X. Ying, H. Wen, W. L. Lu, J. Du, J. Guo, W. Tian, Y. Men, Y. Zhang, R. J. Li, T. Y. Yang, D. W. Shang, J. N. Lou, L. R. Zhang and Q. Zhang, *J. Controlled Release*, 2010, **141**, 183–192.